AIAA JOURNAL
Vol. 33, No. 12, December 1995

Asymmetric Crossing-Shock-Wave/Turbulent-Boundary-Layer Interaction

Doyle D. Knight*
Rutgers University, New Brunswick, New Jersey 08903
T. J. Garrison† and G. S. Settles‡
Pennsylvania State University, University Park, Pennsylvania 16802
and
A. A. Zheltovodov,§ A. I. Maksimov,¶ A. M. Shevchenko,¶ and S. S. Vorontsov**
Institute of Theoretical and Applied Mechanics, Novosibirsk 630090, Russia

A collaborative experimental and theoretical study of the asymmetric crossing-shock-wave/turbulent-boundary-layer interaction is presented. The shock waves are generated by a pair of asymmetric fins that are mounted normal to a flat plate and form a converging channel. The focus of the study is the interaction of the shock waves with the turbulent boundary layer on the flat plate. Two configurations with fin angles 7 × 11 and 15 × 11 deg have been examined at Mach 3.9. Experimental data include surface pressure and heat transfer, adiabatic wall temperature, surface flow visualization, and planar laser scattering images. The computations solve the three-dimensional Reynolds-averaged compressible Navier–Stokes equations incorporating the two equation Chien k–ϵ turbulence model. The computed surface pressure displays good agreement with experiment. The computed and experimental surface pressure and flowfield flow visualization are in general agreement. The computed surface heat transfer displays significant disagreement with experiment. The flowfield manifests a complex shock wave system and a pair of counter-rotating vortices.

I. Introduction

SHOCK-wave/turbulent-boundary-layer interactions occur in a wide range of aeronautical and aerospace systems. Examples include high-speed inlets, nozzles, transonic compressors, rotorcraft, wing-fuselage junctures, and deflection of control surfaces. A full understanding of shock-wave/turbulent-boundary-layer interactions is essential for effective design. Significant progress has been achieved in the understanding of the flow structure for a family of two- and three-dimensional shock-wave/turbulent-boundary-layer interactions, and several flows can now be considered well understood (e.g., the single fin[1,2]). Recent research efforts have concentrated on more complex three-dimensional shock-wave/turbulent-boundary-layer interactions, in particular, the crossing shock (double fin) interaction (Fig. 1) due to applications to high-speed inlets.[3,4]

A detailed compilation of experimental and theoretical (computational) studies of the crossing-shock interaction is presented in Knight et al.[5] Nearly all experimental research has focused on the symmetric crossing-shock interaction. Surface pressure has been obtained in nearly all studies of the symmetric and asymmetric interaction. Surface flow visualization (e.g., kerosene lampblack) was performed in all experiments. Flowfield visualization [e.g., planar laser scattering (PLS)] was conducted in three studies (including one study of the asymmetric crossing shock). Additional quantitative experimental data (e.g., surface skin friction and heat transfer, and flowfield profiles of pitot pressure and static pressure) have been obtained in several cases. There is a significant need for additional experimental data, however, particularly for the asymmetric interaction, including measurements of surface skin friction and heat transfer; flowfield profiles of pitot pressure, yaw angle, and pitch angle; and flowfield visualization.

Previous theoretical (computational) research has focused on the symmetric crossing-shock interaction. The computed flows have shown generally good agreement with experimental data for surface pressure, shock structure, and boundary-layer profiles of pitot pressure and yaw angle, although the level of agreement lessens with increasing shock strength and distance downstream in the interaction. The computed flows have not accurately predicted surface heat transfer or skin friction, however.[6,7]

Collaborative experimental and theoretical research has been crucial to the development of understanding of the flowfield structure of the symmetric crossing-shock interaction. The streamline structure is dominated by a pair of counter-rotating vortices (generated by the individual single fin interactions) that merge at the centerline to form a low total pressure region.[6,8–10] The wave structure encompasses a complex set of multiple shock reflections, expansions, and slip lines.[6,8–14] A complete understanding of the structure of the symmetric crossing-shock interaction has not been achieved, however, and additional research is needed. No flow structure model has been

Received March 13, 1995; revision received Aug. 15, 1995; accepted for publication Aug. 22, 1995.

*Professor, Department of Mechanical and Aerospace Engineering. Associate Fellow AIAA.
†Graduate Research Assistant, Department of Mechanical Engineering; currently Assistant Professor, Mechanical Engineering Department, Louisiana State University, Baton Rouge, LA 70803. Member AIAA.
‡Professor, Department of Mechanical Engineering. Associate Fellow AIAA.
§Senior Research Scientist, Chief of Separated Flows Laboratory. Member AIAA.
¶Research Scientist.
**Research Scientist and Chief of Laboratory.

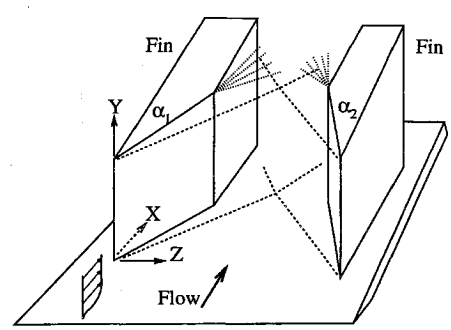

Fig. 1 Crossing shock (double fin).

proposed for the asymmetric crossing-shock interaction, though it may be expected to be somewhat similar to the symmetric model for cases wherein the asymmetry is small.

The objective of this paper is to report on results from a collaborative experimental and theoretical investigation of an asymmetric crossing-shock interaction. This represents the first investigation of an asymmetric crossing-shock interaction. Two configurations were considered at $M_\infty = 3.9$, namely 7 × 11 and 11 × 15 deg, corresponding to the experiments of Zheltovodov et al.[15] and Garrison and Settles.[13]

II. Experiments

Experiments were conducted at the Institute of Theoretical and Applied Mechanics (ITAM), Siberian Division of the Russian Academy of Sciences by Zheltovodov et al., and at the Penn State Gas Dynamics Laboratory by Garrison and Settles. The facilities are described in Refs. 16 and 11, respectively. The experimental configurations for Zheltovodov et al. and Garrison and Settles are presented in Figs. 2 and 3. The location of the inviscid shocks and slip line are indicated. Zheltovodov et al. employed chamfered fins of length 192 mm and height 100 mm, separated by 73.5 mm at the entrance and a minimum throat width of 32 mm. Garrison and Settles employed two straight fins of length 146.1 mm and height 82.5 mm, separated by 96 mm at the entrance.

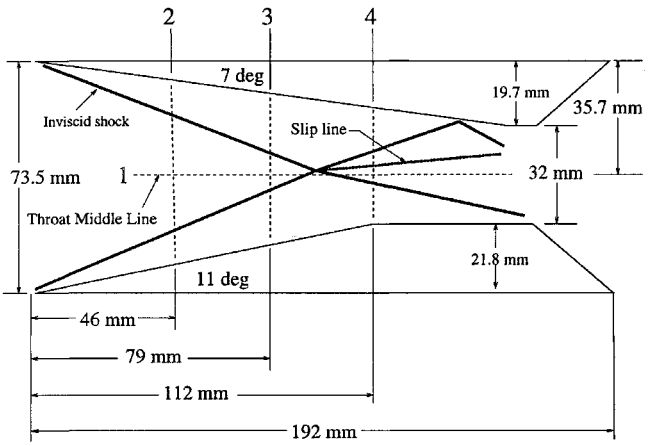

Fig. 2 7 × 11 deg (Ref. 15).

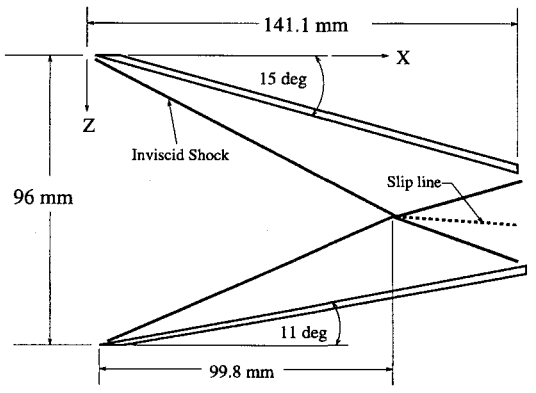

Fig. 3 15 × 11 deg (Ref. 13).

Zheltovodov et al. obtained surface flow visualization, measured surface pressure and heat transfer, adiabatic and heated wall temperatures (using the electric-calorimetry method[15]) at four locations [the throat middle line (TML), and $x = 46$, 79, and 112 mm], and obtained panoramic surface (adiabatic and heated wall) temperatures (using a high-resolution thermovision system[15]). Garrison and Settles obtained surface flow visualization on the flat plate and PLS visualization of the flowfield. The experimental conditions are presented in Table 1. The flat plate and fin surfaces were approximately adiabatic for the experiments of Garrison and Settles.[13] Zheltovodov et al. performed experiments for both adiabatic and nonadiabatic walls.

III. Computations

The theoretical model is the three-dimensional Reynolds-averaged compressible Navier–Stokes equations. Turbulence is represented by the two-equation Jones–Launder (k–ϵ) turbulence model[17] incorporating the low-Reynolds-number modifications of Chien[18] and standard values of the turbulence model constants.[19] The NPARC code[20] was used for 7 × 11 deg (case 1) and the CRAFT code[21] for 11 × 15 deg (case 2). Both codes solve the full three-dimensional Reynolds-averaged compressible Navier–Stokes equations, including the turbulence model equations. The NPARC code employs the Beam–Warming algorithm with explicit and implicit damping. The CRAFT code utilizes Roe's method for the inviscid fluxes and central differencing for the viscous and turbulence source terms. Both methods employ an approximate factorization of the Jacobian.

Two separate computations were performed for case 1 to determine the heat transfer coefficient $C_h = q_w(x, z)/\{\rho_\infty U_\infty c_p[T_w(x, z) - T_{aw}(x, z)]\}$ where $q_w(x, z) = -\kappa_w \partial T/\partial y$ is the wall heat transfer. For case 1a, the wall temperature was fixed $T_w = 1.037 T_{t\infty}$ and the local heat transfer $q_w(x, z)$ determined. For case 1b the wall was assumed adiabatic and the local adiabatic wall temperature $T_{aw}(x, z)$ was determined. This approach has been employed previously for comparison with experimental heat transfer.[22]

Details of the computations are presented in Table 2. The numerical grid accurately resolves the boundary layer (on the flat plate) and inviscid regions based on comparison with previous computations of symmetric crossing-shock interactions wherein grid refinement studies were performed.[9] The thin boundary layers on the fin surfaces were not resolved, and slip boundary conditions were applied at the fin surfaces. Previous studies of the single fin interactions[23] have demonstrated that the shock-wave/turbulent-boundary-layer interaction is essentially unaffected by the boundary layer on the fin. Of course, sufficiently far downstream of the intersection of the crossing shocks, the shocks will interact with the turbulent boundary layers on the sidewall fin surfaces. However, in the present study, nearly all of the experimental data are obtained upstream of the sidewall shock-wave/turbulent-boundary-layer interactions, and consequently the omission of the fin boundary layers does not affect comparison with experiment in this regard. Also, Bardina and Coakley[24] observed that the treatment of the fin boundary layers as laminar or laminar/turbulent affected the flowfield only in the immediate vicinity of the fin/plate junction for a Mach 8.3 crossing-shock interaction. However, in the present study, experimental data

Table 1 Experimental and computational conditions for asymmetric crossing shock[a]

Reference	M_∞	α_1, deg	α_2, deg	$Re_{\delta\infty}$	$p_{t\infty}$, MPa	$T_{t\infty}$, K	δ_∞, mm	δ^*_∞, mm	θ_∞, mm
Experiment									
Zheltovodov et al.[15]	3.95	7	11	3.0×10^5	1.5	260	3.5	1.1	0.13
Garrison and Settles[13]	3.85	15	11	2.6×10^5	1.5	295	3.5	1.1	0.13
Computation									
Cases 1a and 1b	3.85	7	11	3.0×10^5	1.5	270	3.5	1.1	0.13
Case 2	3.85	15	11	2.6×10^5	1.5	295	3.5	1.1	0.15

[a] M_∞ = freestream Mach number; α_1, α_2 = fin angles, deg; $Re_{\delta\infty}$ = Reynolds number based on δ_∞; $p_{t\infty}$ = freestream total pressure; $T_{t\infty}$ = freestream total temperature; δ_∞ = upstream boundary-layer thickness; δ^*_∞ = upstream displacement thickness; and θ_∞ = upstream momentum thickness.

Table 2 Details of computations[a]

Reference	α_1, deg	α_2, deg	T_w	N_x	N_y	N_z
Case 1a	7	11	I	101	68	49
Case 1b	7	11	A	101	68	49
Case 2	15	11	A	97	59	59
	$\Delta x/\delta_\infty$	$\Delta y_{\min}/\delta_\infty$	$\Delta y_{\max}/\delta_\infty$	$\Delta z_{\min}/\delta_\infty$	$\Delta z_{\max}/\delta_\infty$	$\Delta y_2^+\|_{\rm rms}$
Case 1a	0.50	7.64×10^{-5}	0.51	0.20	0.48	0.16
Case 1b	0.50	7.64×10^{-5}	0.51	0.20	0.48	0.19
Case 2	0.50	5.29×10^{-4}	0.51	0.20	0.50	0.77

[a] N_x = number of points in x; N_y = number of points in y; N_z = number of points in z; $\Delta y_2^+|_{\rm rms}$ = rms grid spacing at wall in wall units; I = isothermal wall; and A = adiabatic wall.

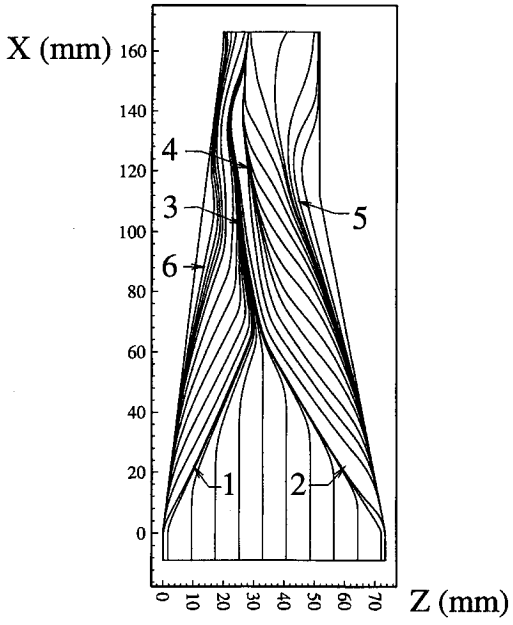

Fig. 4 Computed skin-friction lines for 7 × 11 deg: 1—left incident separation line, 2—right incident separation line, 3—left downstream coalescence line, 4—right downstream coalescence line, and 5 and 6—line of divergence.

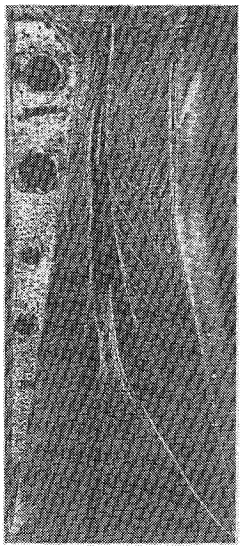

Fig. 5 Experimental surface flow for 7 × 11 deg.

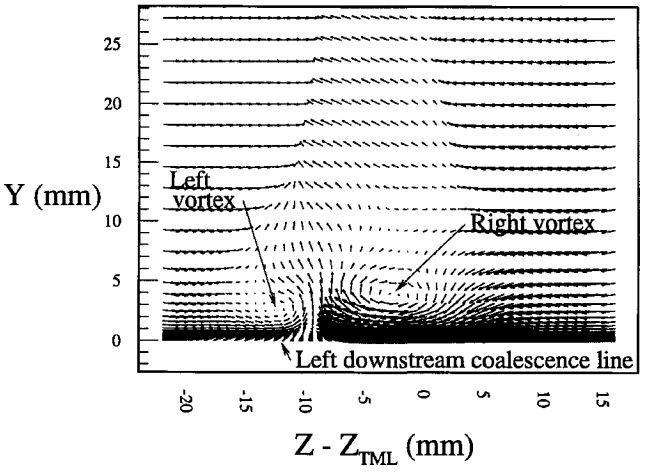

Fig. 6 Crossflow velocity vectors at x = 112 mm for 7 × 11 deg.

are available only in the central portion of the flow, and thus our comparison with experiment is expected to be unaffected by the use of slip boundary conditions on the fins.

The inflow profiles for the three-dimensional Navier–Stokes computations, obtained by a separate boundary-layer calculation using the EDDYBL code,[19] matched the experiment.

IV. Results

A. Crossing Shock 7 × 11 deg

The computed surface skin-friction lines and experimental surface flow visualization are displayed in Figs. 4 and 5, respectively. In comparing these results here (and in the 15 × 11 deg case), two points are noted. First, the computed surface skin-friction lines are typically sensitive to the turbulence model employed,[25] especially in the vicinity of singular points (e.g., nodal and saddle points). Second, the experimental surface flow visualization technique has not been calibrated to the actual mean surface shear stress direction, although Squire[26] provides substantial theoretical basis for concluding the method to be accurate. Notwithstanding these cautionary remarks, the comparison of the computed skin-friction lines and experimental surface flow visualization is helpful in understanding the flowfield streamline structure.

The incident separation lines (lines of coalescence[27]) emanating from the fin leading edges (1 and 2) are clearly evident in the computation and experiment. These separation lines are associated with the incident single fin interactions. The computed and experimental separation line angles, measured relative to the x axis, agree within 10%. The incident separation lines coalesce near the center of the region to form a narrow band of skin-friction lines (3) that is offset to the left side of the channel and is denoted the left downstream coalescence line. This line represents approximately the surface image of the boundary between the left and right vortices generated by the incident single fin interactions. The vortices are evident in the crossflow velocity vectors (Fig. 6) at x = 112 mm. The crossflow velocity vectors near the surface change direction at 3. A second line of coalescence, denoted the right downstream coalescence line (4), forms alongside on the right and farther downstream. It is associated with a secondary separation underneath the left side of the right vortex (see Ref. 5) caused by the spanwise adverse pressure gradient as described later. Lines of divergence are also apparent near the right fin (5) and left fin (6) associated with the incident single fin interaction.

The computed and experimental surface pressure, normalized by the freestream static pressure p_∞, are displayed in Figs. 7 and 8. The uncertainty in the experimental surface pressure measurements is ±0.5%. The four locations (see Fig. 2) are the TML (1) and three

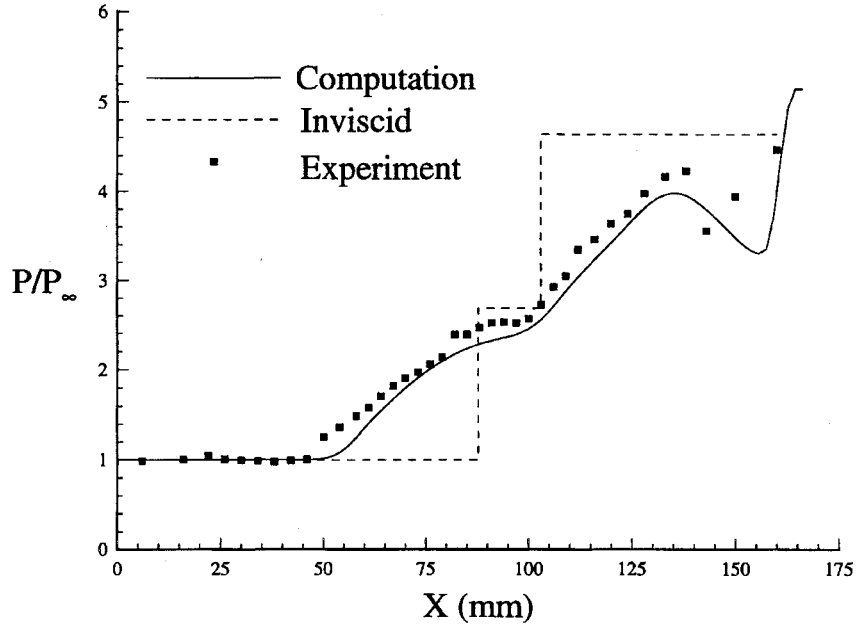

Fig. 7 Wall pressure on TML for 7 × 11 deg.

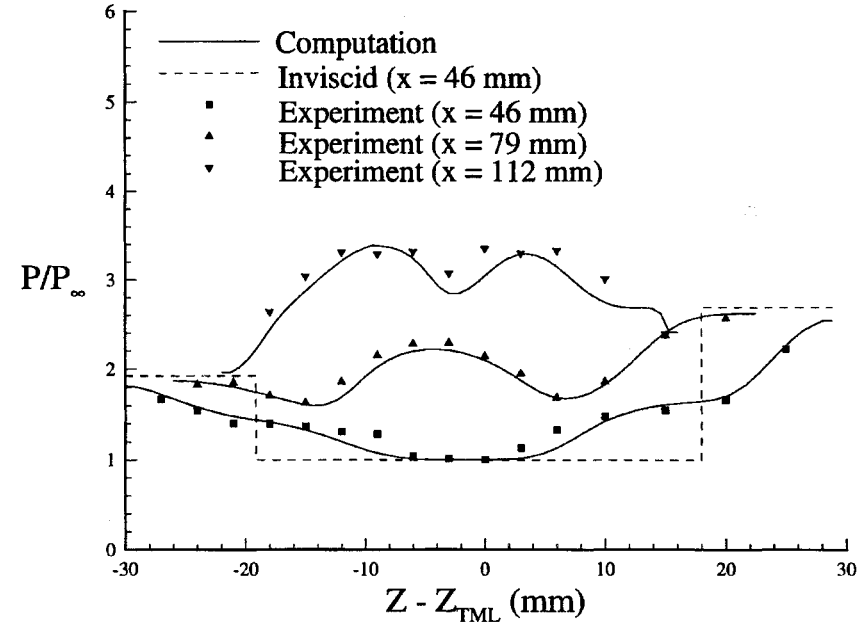

Fig. 8 Wall pressure at x = 46, 79, and 112 mm for 7 × 11 deg.

streamwise locations (2, 3, and 4). The inviscid surface pressure is shown on the TML (up to $x = 160$ mm) and at streamwise location 2. There is an intermediate plateau in the inviscid pressure for 87.7 mm $< x <$ 103.0 mm since the inviscid shock intersection point does not coincide with the TML. The computed and experimental surface pressure on TML are in good agreement for $x < 135$ mm, although the computation underestimates the extent of the upstream influence, as observed in previous studies (e.g., Ref. 8). The computed pressure does not accurately predict the pressure rise (beginning at $x = 145$ mm) associated with the shock reflection from the 7-deg fin, since the computation omits the boundary layers on the fin surfaces. In Fig. 8, the abscissa $z - z_{TML}$ represents the spanwise distance measured from the TML. At $x = 46$ mm, the computed and experimental surface pressure show close agreement. The surface pressure profile corresponds to the individual λ-shock structures generated by the left and right fins.[28,29] At this location, the λ shocks have not intersected. At $x = 79$ mm, the computed and experimental surface pressures exhibit similar close agreement. Although the inviscid shocks have not yet intersected at this location, the forward segments of the individual λ shocks (denoted the separation shock[28]) have reflected from one another as evidenced by the high pressure in the vicinity of the TML. At $x = 112$ mm, the computed and experimental surface pressures are in general agreement. The right downstream coalescence line (4 in Fig. 4) at $x = 112$ mm is located at $z - z_{TML} \approx -7$ mm, coinciding with the adverse spanwise pressure gradient that has caused the secondary separation. Further detail is presented in Ref. 5. (By comparison with Fig. 4, the flow near the surface at $x = 112$ mm and $z - z_{TML} \approx 0$ to -7 mm is moving towards the left fin. Thus, the spanwise pressure gradient in the region -7 mm $< z - z_{TML} < 0$ mm at $x = 112$ mm is adverse.)

The computed and experimental surface heat transfer coefficient C_h is presented in Figs. 9 and 10. The uncertainty in the experimental heat transfer measurements is ±10–15%. The computed T_{aw}, required for the computation of C_h, is within 5% of the experimental measurement (see Ref. 5) obtained using the thermovision technique as well as the thermocouple measurements. Downstream of the intersection of the fin-generated λ-shock structures (i.e., for $x > 90$ mm on the TML) the computations overpredict the heat

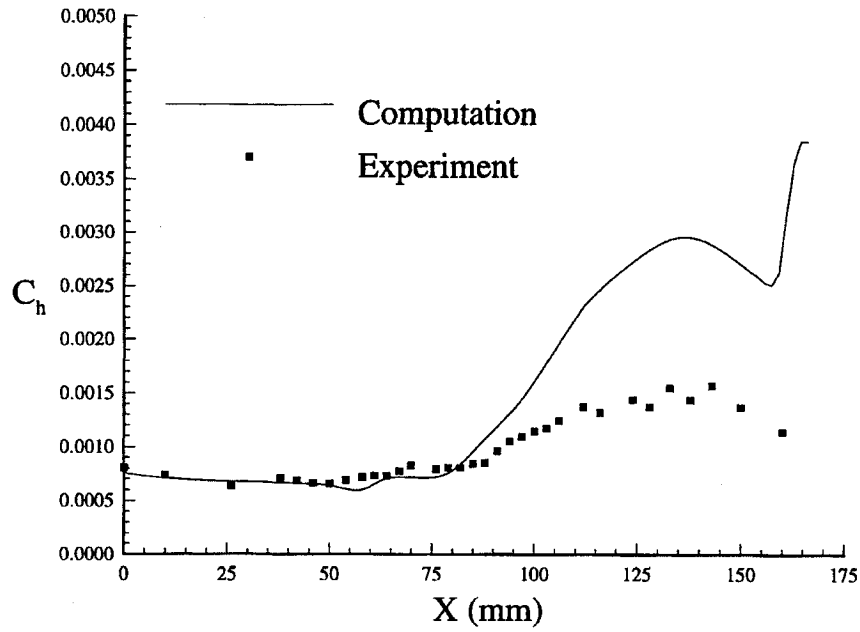

Fig. 9 Heat transfer on TML for 7 × 11 deg.

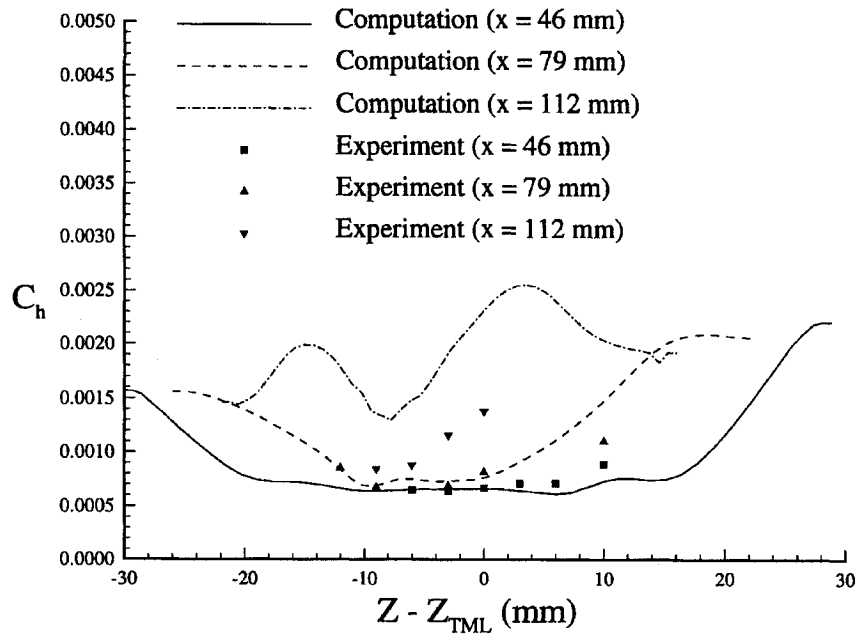

Fig. 10 Heat transfer at x = 46, 79, and 112 mm for 7 × 11 deg.

transfer by approximately a factor of 2. This discrepancy is attributable to the limitations of the turbulence model and is consistent with previous results for the symmetric crossing shock at Mach 8.3 using a similar k–ϵ model.[6] The computed and experimental heat transfer are in close agreement at $x = 46$ and 79 mm (Fig. 10). However, all of the experimental data at $x = 46$ mm and nearly all of the experimental data at $x = 79$ mm are within the undisturbed incoming boundary layer. Comparison of the computed and experimental heat transfer at $x = 112$ mm, located downstream of the intersection of the λ-shock structures, shows significant disagreement. In summary, the computed C_h displays qualitatively the trends observed in the experiment but does not provide reliable values downstream of the interaction of the λ shocks.

The computed mean streamline structure is shown in Fig. 11 together with computed total pressure $p_t/p_{t\infty}$ contours. The first p_t contour shows the initial formation of the individual counter-rotating vortices, as evidenced by the bulge in low p_t contours. These vortices collide to form a counter-rotating vortex pair characterized by low total pressure and low Mach number. The right vortex (as viewed looking downstream) is significantly larger due to the larger initial pressure rise associated with the right (11-deg) fin compared with the left (7-deg) fin. The vortex pair moves towards the left fin consistent with the direction of the inviscid flow downstream of the inviscid shock intersection. The vortex pair entrains the low energy fluid in the incoming boundary layer into a concentrated region. The principal difference between the asymmetric and symmetric mean streamline pattern[6,8,9] is the asymmetric location of the counter-rotating pair.

B. Crossing Shock 15 × 11 deg

The computed skin-friction lines and experimental surface flow visualization for the 15 × 11 deg configuration are presented in Figs. 12–14, respectively. The separation lines originating from the fin leading edges are apparent in the computation and experiment. The computed and experimental separation line angles agree within 7%. The computed skin-friction lines show a node-saddle pattern in

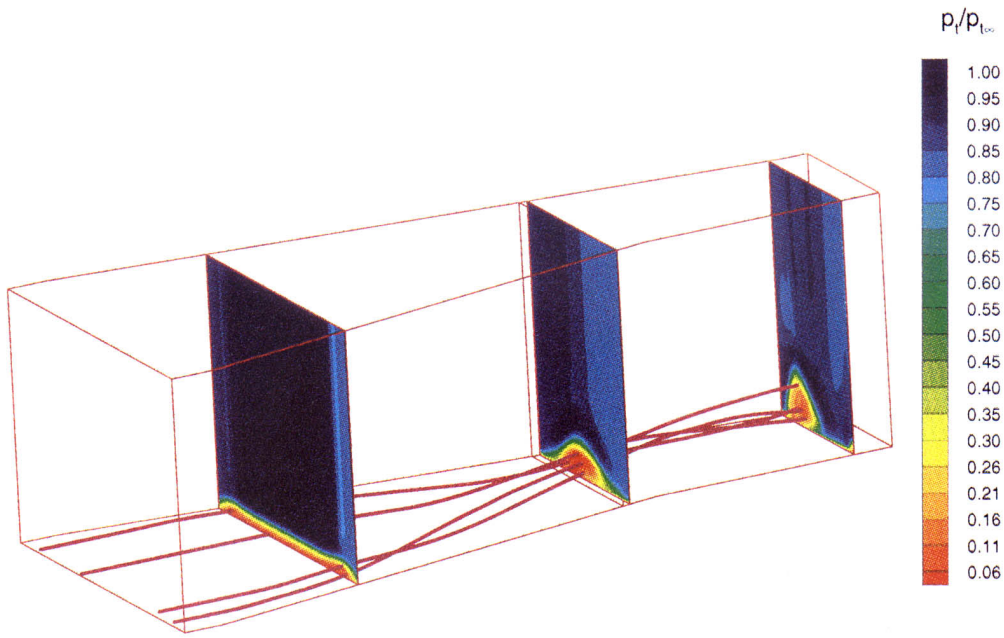

Fig. 11 Flowfield structure for 7 × 11 deg.

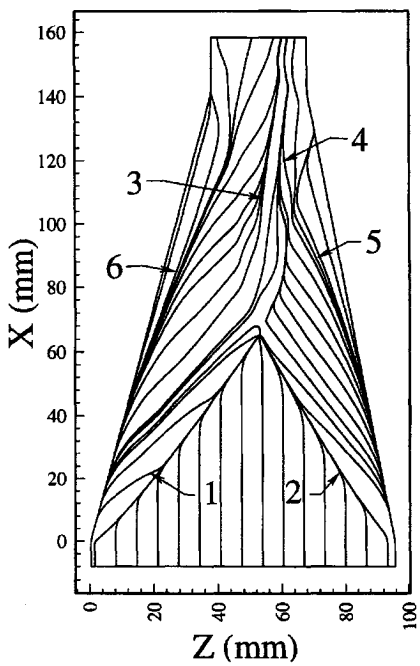

Fig. 12 Computed skin-friction lines for 15 × 11 deg (see Fig. 4 for legend).

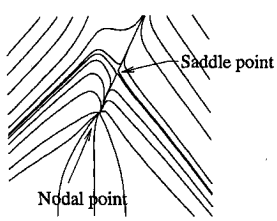

Fig. 13 Computed skin-friction lines for 15 × 11 deg near nodal point.

the vicinity of the intersection of the separation lines (Fig. 13). Two lines of coalescence form downstream in qualitative agreement with experiment and the 7 × 11 deg case. The role of 3 and 4 is opposite to the 7 × 11 deg configuration, of course, since the larger fin is on the left.

Experimental PLS images are displayed in Figs. 15–17 at x = 85.1, 102.9, and 120.7 mm. Figure 15 corresponds to a location

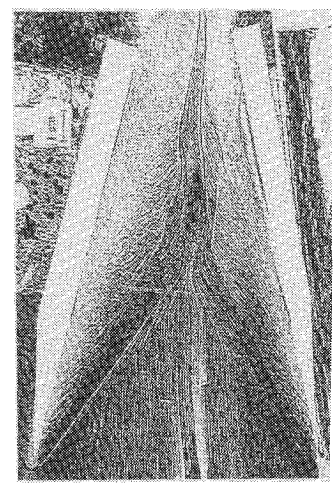

Fig. 14 Experimental surface flow for 15 × 11 deg.

upstream of the inviscid shock intersection (see Fig. 3), although it is downstream of the intersection of the separation shocks associated with the λ shocks generated by the fins. Figure 16 is immediately downstream of the inviscid shock intersection, and Fig. 17 is further downstream. The PLS images were obtained by a miniature videocamera, located downstream of the crossing-shock interaction, which imaged the interaction in the upstream direction. Consequently, the 15-deg fin is on the right side in the PLS images. Computed static pressure contours, normalized by p_∞, are presented in Figs. 18–20, at the same three locations as the PLS images. The static pressure contours have been reversed (i.e., the 15-deg fin is on the right side) to conform with the orientation of the PLS images. The inviscid shocks are evident in the vertical clustering of the contour lines. The principal features of the shock structure at the same three locations, deduced from the experiment and computation, are presented in Figs. 21–23 and are discussed next.

At x = 85.1 mm, the PLS image and pressure contours (Figs. 15 and 18) display the shock structure associated with the initial reflection of the separation shock wave segments. The principal features are shown in Fig. 21 and include the separation shock (2), rear shock (3), reflected separation shock (4), and centerline shock (5). These features are physically the same as described by Garrison et al.[10] and Garrison and Settles[11] for the symmetric crossing-shock interaction. The asymmetry of the incident shocks affects an expected asymmetry in the interaction shock structure. The cross sections of

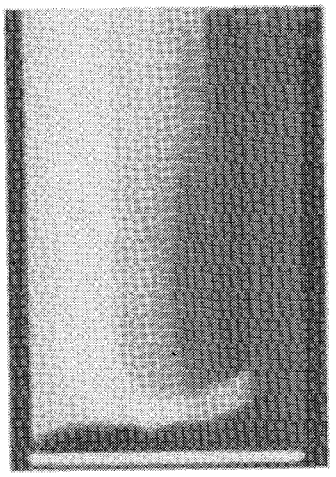

Fig. 15 Experimental PLS at x = 85.1 mm for 15 × 11 deg.

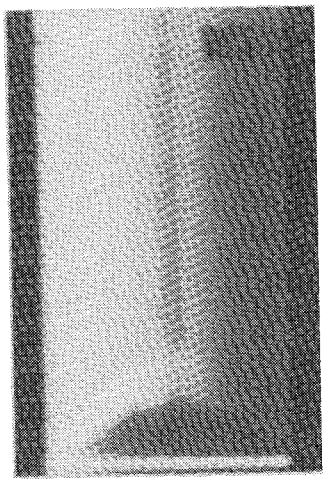

Fig. 16 Experimental PLS at x = 102.9 mm for 15 × 11 deg.

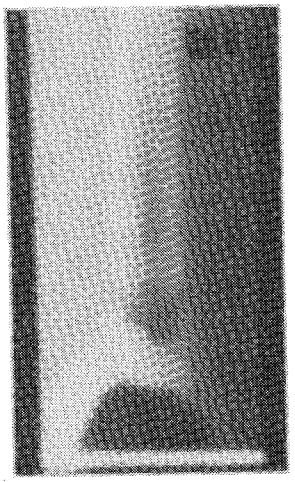

Fig. 17 Experimental PLS at x = 120.7 mm for 15 × 11 deg.

the small (6) and large (7) vortices are shown schematically. Note that the larger vortex is on the right, corresponding to the 15-deg fin. The vortices are counter-rotating. In this view, the large vortex rotates clockwise, and the small vortex counterclockwise.

At x = 102.9 mm, the PLS image and pressure contours (Figs. 16 and 19) display a strong asymmetric shock structure. In Fig. 22, the reflected separation shock on the left side (4) is significantly stronger than its counterpart on the right, as may be anticipated based upon the asymmetry of the inviscid flow (i.e., the reflected inviscid shock on the left in Fig. 19 is stronger than its counterpart on the right). Neither the computation nor the experiment has sufficient resolution to distinguish the reflected separation shock on the right from the rear shocks (8). An imbedded shock appears within the

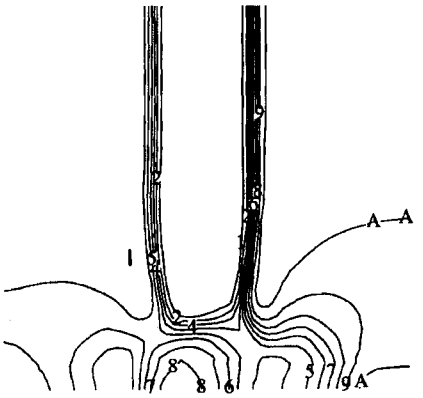

Level	P/P_∞
A	3.50
9	3.25
8	3.00
7	2.75
6	2.50
5	2.25
4	2.00
3	1.75
2	1.50
1	1.25

Fig. 18 Computed pressure at x = 85.1 mm for 15 × 11 deg. The 15-deg fin is on the right.

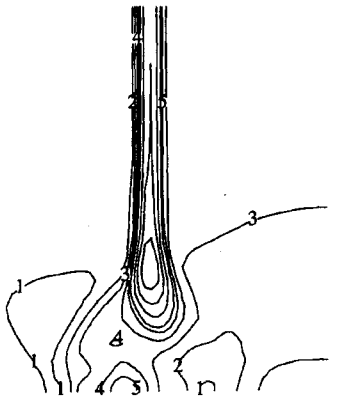

Level	P/P_∞
9	8.00
8	7.00
7	6.00
6	5.00
5	4.50
4	4.00
3	3.50
2	3.00
1	2.50

Fig. 19 Computed pressure at x = 102.9 mm for 15 × 11 deg. The 15-deg fin is on the right.

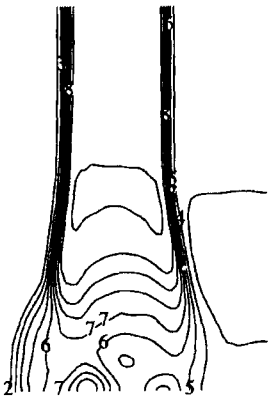

Level	P/P_∞
B	8.00
A	7.00
9	6.50
8	6.00
7	5.50
6	5.00
5	4.50
4	4.00
3	3.50
2	3.00
1	2.50

Fig. 20 Computed pressure at x = 120.7 mm for 15 × 11 deg. The 15-deg fin is on the right.

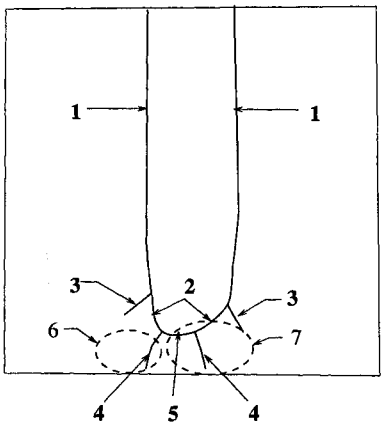

Fig. 21 Wave structure at x = 85 mm for 15 × 11 deg: 1—incident inviscid shock, 2—separation shock, 3—rear shock, 4—reflected separation shock, 5—centerline shock, 6—small vortex, and 7—large vortex. The 15-deg fin is on the right.

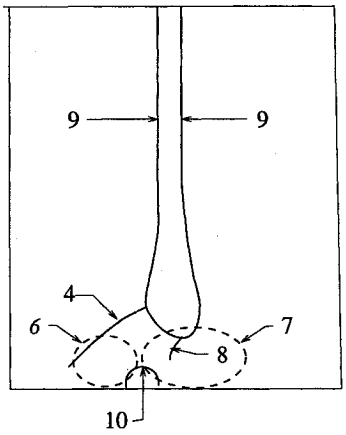

Fig. 22 Wave structure at x = 102.9 mm for 15 × 11 deg: 4—reflected separation shock, 6—small vortex, 7—large vortex, 8—reflected separation shock [or possibly rear shock(s)], 9—reflected inviscid shock, and 10—embedded shock. The 15-deg fin is on the right.

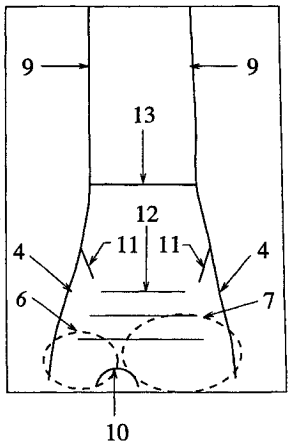

Fig. 23 Wave structure at x = 120.7 mm for 15 × 11 deg: 4—reflected separation shock, 6—small vortex, 7—large vortex, 9—reflected inviscid shock, 10—embedded shock, 11—reflected rear shock, 12—expansion fan, and 13—centerline shock. The 15-deg fin is on the right.

boundary layer (10) in the computations, similar to observations at Mach 8.3 (see Refs. 6 and 9). The experimental PLS images do not provide any detail in the region of the computed embedded shock due to the absence of scattering particles. The cross section of the counterrotating vortex pair (6, 7) has increased due to entrainment from the boundary layer.

At x = 120.7 mm, the PLS image and pressure contours (Figs. 17 and 20) display the continued evolution of the shock structure. In Fig. 23, the reflected separation shocks (4) have moved further towards the fins. The reflected rear shocks (11) are evident in the PLS images; however, they are evidently too weak and small to be resolved accurately by the computations. The imbedded shock wave (10) is again evident in the computations, as indicated in the closeup, Fig. 24, which also displays the numerical grid. An expansion region (12), observed in previous computations[6,8,9] from Mach 3 to 8.3, is evident within the boundary layer. A weak centerline shock (13) is also evident. The counterrotating vortex pair (6, 7) has continued to grow in size.

The basic shock structure described previously is applicable to the 7 × 11 deg configuration also, with due consideration for the orientation of the fins (i.e., the larger fin angle is on the right). However, there does not appear to be an imbedded shock in the 7 × 11 deg case, likely due to the weaker shock strengths. Both the experimental technique (PLS) and computation have limitations on resolution of the flowfield structure, and the preceding description should not be considered complete.

V. Conclusions

A collaborative experimental and theoretical (computational) study of the asymmetric crossing-shock-wave/turbulent-boundary-layer interaction has been performed. Two configurations, 7 × 11 and 15 × 11 deg, have been examined at Mach 3.9. Experimental data include surface pressure and heat transfer, adiabatic wall temperature, surface flow visualization, and PLS images of the flowfield. The computations employ the three-dimensional Reynolds-averaged compressible Navier–Stokes equations with turbulence represented by the two-equation k–ϵ model.

The principal conclusions are as follows.

The computed surface pressure displays good agreement with experiment.

The computed surface skin-friction lines and experimental surface flow visualization display close agreement in the location of the initial separation lines and are in qualitative agreement within the crossing-shock interaction region.

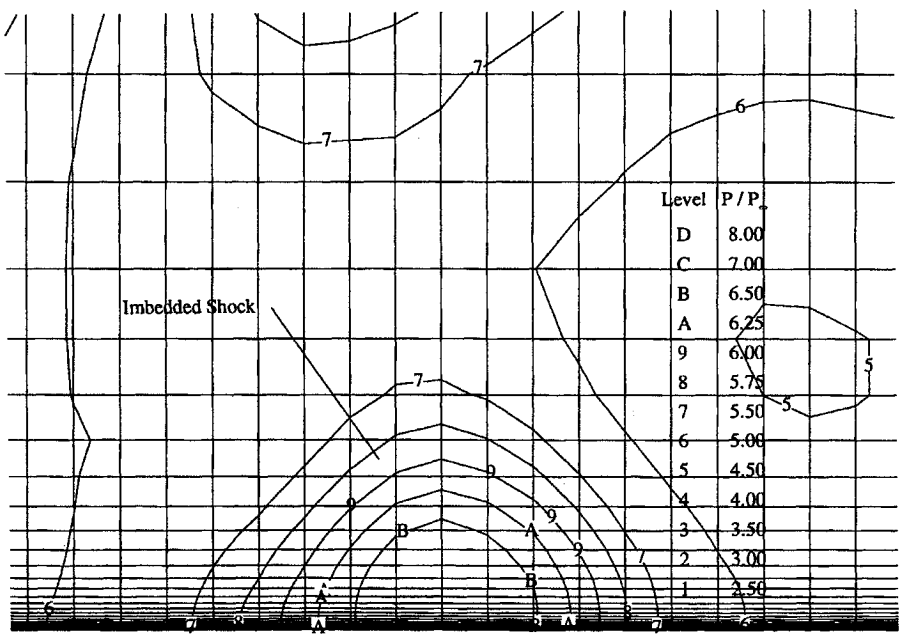

Fig. 24 Computed pressure at x = 120.7 mm for 15 × 11 deg.

The computed heat transfer is in error by approximately a factor of 2 within the region downstream of the intersection of the λ shocks generated by the fins. The disagreement may be attributable to limitations in the k–ϵ turbulence model.

The experimental flowfield visualization and computed flowfields define the principal features of the flowfield structure. These include a complex reflected shock structure (qualitatively similar to that of the symmetric crossing-shock interaction), an embedded shock within the boundary layer observed in the computations for the 15×11 deg configuration, and a counter-rotating vortex pair responsible for significant distortion in the total pressure at the outflow. Additionally, the relation of the vortex pair to the surface flow visualization is described.

Acknowledgments

This research was supported by the U.S. Air Force Office of Scientific Research under Grants F49620-93-1-0005 and 89-0315, monitored by Len Sakell; a grant of High Performance Computing time from the Department of Defense HPC Center U.S. Army Engineers Waterways Experiment Station; United Technologies Research Corporation, monitored by Michael Werle; and the Siberian Branch of the Russian Academy of Sciences. Postprocessing of the computations was performed at the Rutgers College of Engineering Supercomputer Remote Access Center. The authors acknowledge, with sincere appreciation, the assistance of Tina Fuchs, Patrick McPartland, and Robert Schwarz in the preparation of several figures. The authors express appreciation to Sanford Dash, Robert Lee, Neeraj Sinha, and Brian York for the use of the CRAFT code.

References

[1]Degrez, G. (ed.), "AGARD Special Course on Shock-Wave/Turbulent Boundary-Layer Interactions in Supersonic and Hypersonic Flow," AGARD Rept. 792, Aug. 1993.

[2]Zheltovodov, A., Borisov, A., Knight, D., Horstman, C., and Settles, G., "The Possibilities of Numerical Simulation of Shock Waves/Boundary Layer Interaction in Supersonic and Hypersonic Flows," *Proceedings of the International Conference on Methods of Aerophysical Research*, Russian Academy of Sciences, Siberian Division, Novosibirsk, 1992, pp. 164–170.

[3]Edwards, C., "A Forebody Design Technique for Highly Integrated Bottom-Mounted Scramjets with Application to a Hypersonic Research Airplane," NASA TN D-8369, Dec. 1976.

[4]Sakell, L., Knight, D., and Zheltovodov, A. (eds.), *Proceedings of the AFOSR Workshop on Fluid Dynamics of High Speed Inlets*, Dept. of Mechanical and Aerospace Engineering, Rutgers Univ., New Brunswick, NJ, 1994.

[5]Knight, D., Garrison, T., Settles, G., Zheltovodov, A., Maksimov, A., Shevchenko, A., and Vorontsov, A., "Asymmetric Crossing Shock Wave-Turbulent Boundary Layer Interaction," AIAA Paper 95-0231, Jan. 1995.

[6]Narayanswami, N., Horstman, C., and Knight, D., "Computation of Crossing Shock Turbulent Boundary Layer Interaction at Mach 8.3," *AIAA Journal*, Vol. 31, No. 8, 1993, pp. 1369–1376.

[7]Garrison, T., Settles, G., Narayanswami, N., and Knight, D., "Laser Interferometer Skin Friction Measurements of Crossing Shock Wave/Turbulent Boundary Layer Interactions," *AIAA Journal*, Vol. 32, No. 6, 1994, pp. 1234–1241.

[8]Narayanswami, N., Knight, D., Bogdonoff, S., and Horstman, C., "Interaction Between Crossing Oblique Shocks and a Turbulent Boundary Layer," *AIAA Journal*, Vol. 30, No. 8, 1992, pp. 1945–1952.

[9]Narayanswami, N., Knight, D., and Horstman, C., "Investigation of a Hypersonic Crossing Shock Wave/Turbulent Boundary Layer Interaction," *Shock Waves*, Vol. 3, No. 1, 1993, pp. 35–48.

[10]Garrison, T., Settles, G., Narayanswami, N., and Knight, D., "Structure of Crossing-Shock Wave/Turbulent Boundary Interactions," *AIAA Journal*, Vol. 31, No. 12, 1993, pp. 2204–2211.

[11]Garrison, T., and Settles, G., "Flowfield Visualization of Crossing Shock-Wave/Boundary Layer Interactions," AIAA Paper 92-0750, Jan. 1992.

[12]Garrison, T., and Settles, G., "Interaction Strength and Model Geometry Effects on the Structure of Crossing-Shock Wave/Turbulent Boundary-Layer Interactions," AIAA Paper 93-0780, Jan. 1993.

[13]Garrison, T., "The Interaction Between Crossing-Shock Waves and a Turbulent Boundary Layer," Ph.D. Thesis, Dept. of Mechanical Engineering, Pennsylvania State Univ., University Park, PA, 1994.

[14]Garrison, T., Settles, G., Narayanswami, N., and Knight, D., "Comparison of Flowfield Surveys and Computations of a Crossing-Shock Wave/Boundary-Layer Interaction," AIAA Paper 94-2273, June 1994; see also *AIAA Journal* (to be published).

[15]Zheltovodov, A., Maksimov, A., Shevchenko, A., Vorontsov, S., and Knight, D., "Experimental Study and Computational Comparison of Crossing Shock Wave-Turbulent Boundary Layer Interaction," *Proceedings of the International Conference on Methods of Aerophysical Research—Part 1*, Russian Academy of Sciences, Siberian Division, 1994, pp. 221–230.

[16]Lokotko, A., and Shushpanov, M., "Heat Aerodynamics Facility T-333," Aerophysical Researches, Inst. of Theoretical and Applied Mechanics, USSR Academy of Sciences, Siberian Division, Novosibirsk, 1972, pp. 18–20.

[17]Jones, W., and Launder, B., "The Prediction of Laminarization with a Two-Equation Model of Turbulence," *International Journal of Heat and Mass Transfer*, Vol. 15, 1972, pp. 301–304.

[18]Chien, K.-Y., "Predictions of Channel and Boundary Layer Flows with a Low Reynolds Number Turbulence Model," *AIAA Journal*, Vol. 20, No. 1, 1982, pp. 33–38.

[19]Wilcox, D., *Turbulence Modelling for CFD*, DCW Industries, La Cañada, CA, 1993.

[20]Cooper, G., and Sirbaugh, J., "PARC Code: Theory and Usage," Arnold Engineering and Development Center, AEDC-TR-89-15, Arnold AFB, TN, Dec. 1989.

[21]Molvik, G., and Merkle, C., "A Set of Strongly Coupled, Upwind Algorithms for Computing Flows in Chemical Nonequilibrium," AIAA Paper 89-0199, Jan. 1989.

[22]Lee, Y., Settles, G., and Horstman, C., "Heat Transfer Measurements and CFD Comparison of Swept Shock Wave/Boundary Layer Interactions," AIAA Paper 92-3665, July 1992.

[23]Knight, D., Badekas, D., Horstman, C., and Settles, G., "Quasi-Conical Flowfield Structure of the Three-Dimensional Single Fin Interaction," *AIAA Journal*, Vol. 30, No. 12, 1992, pp. 2809–2816.

[24]Bardina, J., and Coakley, T., "Three-Dimensional Navier–Stokes Simulations with Two Equation Turbulence Models of Intersecting Shock Waves/Turbulent Boundary Layer at Mach 8.3," AIAA Paper 94-1905, June 1994.

[25]Narayanswami, N., Horstman, C., and Knight, D., "Numerical Simulation of Crossing Shock/Turbulent Boundary Layer Interaction at Mach 8.3—Comparison of Zero- and Two-Equation Turbulence Models," AIAA Paper 93-0779, Jan. 1993.

[26]Squire, L., "The Motion of a Thin Oil Sheet Under the Steady Boundary Layer on a Body" *Journal of Fluid Mechanics*, Vol. 11, Sept. 1961, pp. 161–179.

[27]Rosenhead, L. (ed.), *Laminar Boundary Layers*, Oxford Univ. Press, New York, 1963, pp. 46–113.

[28]Alvi, F., and Settles, G., "Physical Model of the Swept Shock/Boundary Layer Interaction Flowfield," *AIAA Journal*, Vol. 30, No. 9, 1992, pp. 2252–2258.

[29]Zheltovodov, A., and Shilein, E., "3-D Swept Shock Waves/Turbulent Boundary Layer Interaction in Angles Configuration" (in Russian), Inst. of Theoretical and Applied Mechanics, Russian Academy of Sciences, Siberian Division, Preprint No. 34-86, 1986.